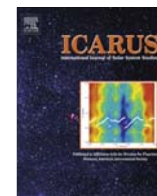




Contents lists available at ScienceDirect

Icarus

journal homepage: www.elsevier.com/locate/icarus

Evidence for the sequestration of hydrogen-bearing volatiles towards the Moon's southern pole-facing slopes

T.P. McClanahan^{a,*}, I.G. Mitrofanov^c, W.V. Boynton^b, G. Chin^a, J. Bodnarik^b, G. Droege^{b,1}, L.G. Evans^{a,e}, D. Golovin^c, D. Hamara^b, K. Harshman^b, M. Litvak^c, T.A. Livengood^{a,d}, A. Malakhov^c, E. Mazarico^a, G. Milikh^d, G. Nandikotkur^g, A. Parsons^a, R. Sagdeev^d, A. Sanin^c, R.D. Starr^{a,f}, J.J. Su^d, J. Murray^d

^a Solar System Exploration Division, NASA Goddard Space Flight Center, Greenbelt, MD 20771, USA

^b Lunar and Planetary Laboratory, University of Arizona, Tucson, AZ 85719, USA

^c Institute for Space Research, RAS, Moscow 117997, Russian Federation

^d University of Maryland, College Park, MD 20742, USA

^e Computer Sciences Corporation, Lanham, MD 20706, USA

^f Catholic University of America, Washington DC 20064, USA

^g School of Natural Sciences, Fairleigh Dickinson University, Teaneck, NJ 07666, USA

ARTICLE INFO

Article history:

Received 14 February 2014

Revised 27 September 2014

Accepted 2 October 2014

Available online xxx

Keywords:

Moon

Ices

Moon, surface

Regoliths

ABSTRACT

The Lunar Exploration Neutron Detector (LEND) onboard the Lunar Reconnaissance Orbiter (LRO) detects a widespread suppression of the epithermal neutron leakage flux that is coincident with the pole-facing slopes (PFS) of the Moon's southern hemisphere. Suppression of the epithermal neutron flux is consistent with an interpretation of enhanced concentrations of hydrogen-bearing volatiles within the upper meter of the regolith. Localized flux suppression in PFS suggests that the reduced solar irradiation and lowered temperature on PFS constrains volatility to a greater extent than in surrounding regions. Epithermal neutron flux mapped with LEND's Collimated Sensor for Epithermal Neutrons (CSETN) was analyzed as a function of slope geomorphology derived from the Lunar Orbiting Laser Altimeter (LOLA) and the results compared to co-registered maps of diurnally averaged temperature from the Diviner Lunar Radiometer Experiment and an averaged illumination map derived from LOLA. The suppression in the average south polar epithermal neutron flux on equator-facing slopes (EFS) and PFS (85–90°S) is $3.3 \pm 0.04\%$ and $4.3 \pm 0.05\%$ respectively (one-sigma-uncertainties), relative to the average count-rate in the latitude band 45–90°S. The discrepancy of $1.0 \pm 0.06\%$ between EFS and PFS neutron flux corresponds to an average of ~ 23 parts-per-million-by-weight (ppmw) more hydrogen on PFS than on EFS. Results show that the detection of hydrogen concentrations on PFS is dependent on their spatial scale. Epithermal flux suppression on large scale PFS was found to be enhanced to $5.2 \pm 0.13\%$, a discrepancy of ~ 45 ppmw hydrogen relative to equivalent EFS. Enhanced poleward hydration of PFS begins between 50°S and 60°S latitude. Polar regolith temperature contrasts do not explain the suppression of epithermal neutrons on pole-facing slopes. The [Supplemental on-line materials](#) include supporting results derived from the uncollimated Lunar Prospector Neutron Spectrometer and the LEND Sensor for Epithermal Neutrons.

Published by Elsevier Inc. This is an open access article under the CC BY-NC-ND license (<http://creativecommons.org/licenses/by-nc-nd/3.0/>).

1. Introduction

After years of research the ongoing quest to quantify the spatial distribution of the Moon's hydrogen-bearing volatiles remains an intriguing and open question for lunar scientists. The long standing objective to understand the nature of volatiles and their surface

distributions comes from the ongoing in-situ resource knowledge gaps that must be addressed to effectively plan future lunar surface missions (Lofgren, 1993; Sanders and Larson, 2010). For decades there was a polar focus, driven by the dominant theory that held that the Moon's extreme vacuum and thermal conditions precluded the near-surface existence of hydrogen-bearing volatiles, except in the cryogenically stable permanently shadowed regions (PSR) (Urey, 1952; Watson et al., 1961; Arnold, 1979). These studies suggested hydrogen-bearing volatiles could be cold-trapped in the PSR's and accumulated over billions of years of lunar history by the combined effects of highly constrained sublimation rates and

* Corresponding author at: Building 34, Rm W218, Code 691, NASA Goddard Space Flight Center, Greenbelt, MD 20771, USA.

E-mail address: timothy.p.mcclanahan@nasa.gov (T.P. McClanahan).

¹ Deceased.

the episodic influx of meteorites or comets. However, in 2009 discoveries from the Chandrayaan-1, Deep Impact and Cassini missions forced scientists to consider the possibility of a much more complicated volatile environment in which hydrogen-bearing volatiles are more prevalent and active on the lunar surface than previously thought (Goswami and Annadurai, 2008; Pieters et al., 2009; Clark, 2009; Sunshine et al., 2009). Their jointly released results from near infra-red (NIR) spectroscopy of the 3 μm absorption line associated with hydroxyl and/or water suggested that there is an active and widespread hydration of the lunar surface. Exogenously sourced hydroxyl and water may be produced on the lunar surface by solar wind driven and proton-induced hydroxylation of regolith silicates that may be subsequently ballistically transported in bombardment processes (Starukhina, 2000; Crider and Vondrak, 2000, 2002; McCord et al., 2011). From these results, the static, PSR-centric perspective of lunar hydrogen volatiles is now evolving to comprehend new and more complex dynamics that have and are driving the Moon's hydrogen-bearing volatiles.

Several results have partially proven the PSR hypothesis. Initial Clementine bistatic radar observations of the poles were inconclusive that found surface circular polarization ratios that were consistent with an interpretation of water ice in some PSR's, but were later refuted (Nozette et al., 1996; Simpson and Tyler, 1999; Fa et al., 2011). Results from the late 1990's era Lunar Prospector Neutron Spectrometer (LPNS) showed, using image reconstruction techniques applied to epithermal neutron flux maps, that some south polar PSR's had regional signatures of enhanced concentrations of hydrogenous materials (Feldman et al., 1998; Elphic et al., 2007). More recently, the Lunar Reconnaissance Orbiter's (LRO) Lunar Exploration Neutron Detector (LEND) found significant suppressions in the epithermal neutron flux consistent with hydrogen-bearing materials within the PSR's of several craters e.g. Cabeus and Shoemaker (Chin et al., 2007; Vondrak et al., 2010; Mitrofanov et al., 2010a, 2010b; Boynton et al., 2012; Sanin et al., 2012). Far ultra-violet (FUV) observations of the Moon's polar Lyman- α albedo by LRO's LAMP instrument suggested ~ 1 –2% water frost on the regolith of several south polar PSR's (Gladstone et al., 2012). Results from LRO's Lunar Observing Laser Altimeter albedo (LOLA) were used to suggest deposits of surface water frost on the walls of Shackleton crater using 1064 nm albedo measurements (Smith et al., 2010; Zuber et al., 2012). Lucey et al. (2014) found LOLA albedo differences that are consistent with an interpretation of water frost deposition in PSR vs. non-PSR and on pole-facing slopes (PFS) vs. equator-facing slopes (EFS). Ground truth evidence of the existence of hydrogen-bearing materials within a south polar PSR was established by the NIR and ultra-violet (UV) detection of water and molecular hydrogen within the excavated plume made by the exhausted rocket motor of the Lunar CRater Observing and Sensing Satellite (LCROSS) as it impacted Cabeus crater (Colaprete et al., 2010; Hurley et al., 2012).

Several lines of evidence support the hypothesis that surface hydration may be occurring outside the PSR's. Theoretical studies suggest that the extreme end-member cryogenic temperatures < 100 K in the polar PSR's may be not provide the optimal thermal conditions for the entrainment of hydrogen-bearing volatiles (Siegler et al., 2011; Schorghofer and Taylor, 2007). LEND found that the epithermal neutron flux was significantly suppressed in some polar regions outside PSR's, inferring the presence of hydrogen-bearing materials in regions that regularly experience some level of solar irradiation (Mitrofanov et al., 2012). Beginning in the mid-latitudes, results from NIR spectroscopy, far ultra-violet (FUV) and epithermal neutron observations indicate trends that are consistent with the interpretation poleward increases in hydrogen concentration (Feldman et al., 1998; McCord et al., 2011; Gladstone et al., 2012; Litvak et al., 2012; Hendrix et al., 2012; Li

et al., 2012). From LEND results, Mitrofanov et al. (2012) postulated a correlation between the poleward decrease in the epithermal neutron flux and solar irradiation.

There is also evidence that topography, aside from the polar basins that contain the PSR's, has an active role in biasing the locations of volatile spatial distributions. NIR results from the Moon Mineralogy Mapper on Chandrayaan-1 identified diurnally shifting hydrogen-bearing materials that moved through the day towards low illumination conditions on the slopes of mid-latitude craters (Pieters et al., 2009). Cheek et al. (2011) found evidence in NIR spectroscopy measurements that surface hydroxyl or water concentrations were enhanced in the upper latitude Golschmidt crater, 73°N 3.8°W. However, enhanced hydrogen concentrations were not detected in the analysis of LPNS epithermal neutron flux associated with Golschmidt indicating the hydrogen deposits are likely associated with the top few microns of the surface (Lawrence et al., 2011).

This research explores the possibility that the Moon's topography creates locally stable pockets of hydrogen-bearing volatiles in the persistently low solar irradiation and temperature conditions found on PFS. Nearly ~ 4.5 years of high resolution observations from LEND's Collimated Sensor for Epithermal Neutrons (CSETN) collected over the Moon's south polar region at 30–50 km altitude are correlated with fully-registered topography and average illumination maps derived from LOLA as well as an average surface temperature map produced by the Diviner Lunar Radiometer Experiment (Diviner) (Paige et al., 2010a, 2010b). LOLA topography is decomposed as a function of the three principal factors that govern the Moon's insolation including: latitude, slope and slope aspect (Smith et al., 2010). By averaging the fully registered maps as a function of these primary insolation factors, the averaged areas are increased and the statistical significance of the results is enhanced. Localized contrasts of averaged epithermal neutron flux, illumination and temperature on pole and equator-facing slopes (EFS) illustrate their respective correlation to insolation.

This work shows that:

- The suppression of the epithermal neutron flux on PFS is substantially greater than on equivalent EFS, which supports the hypothesis that local concentrations of hydrogen are biased towards PFS.
- The biased hydration of PFS is a widespread phenomenon in the Moon's southern latitudes.
- The contrast between the EFS and PFS epithermal neutron flux and the inference for the hydration of pole-facing surfaces extends from about 50°S latitude to the south pole.
- The magnitude of the epithermal neutron flux suppression increases with the spatial scale of PFS, but not EFS in the upper-latitudes. The result suggests that a hydrogen contrast exists for PFS with respect to their surroundings and that EFS are hydrated to levels that are in equilibrium with their surroundings.
- Regolith temperature contrasts appear to be ruled out as the cause of the localized suppression of epithermal neutron flux on pole-facing slopes.

Section 2 reviews the paper's primary hypothesis and uses a Martian example to illustrate the characteristics of a pattern of hydration on crater slopes. The section also describes the implications for hydrogen detection by orbital neutron and temperature remote sensing of lunar slopes. Section 3 illustrates the south polar averaged epithermal neutron flux, temperature, illumination and topography maps used in this study. Analytical methods are also described. Section 4 reviews several results from the correlated studies of epithermal flux, illumination, topography and tempera-

ture. Section 5 discusses the relevance of the findings to hydrogen volatiles research and Section 6 reviews the paper's conclusions.

2. Background

The primary hypothesis for this research is that a combination of latitude and topographic factors that principally govern insolation create a ubiquitous pattern of slope hydration that is correlated with the Moon's heavily cratered surface (Carruba and Coradini, 1999). The pattern is consistent with insolation driven hydration patterns on the terrain of Earth and Mars where topographic relief modulates solar flux, the surface temperature and the near surface spatial distributions of water (Geiger et al., 1965; Vincendon et al., 2010). Key differences are that the dynamics of volatile processes on the Moon are likely quite different from Earth and Mars, given the Moon's extreme vacuum and consequent lack of convective processes, differing species, differing mechanisms for volatile production and destruction, differing surface residence time and transport processes. However, regardless of how exogenously sourced hydrogen-bearing volatiles may be delivered to the surface, we postulate that the thermodynamics of loss processes govern hydrogen-bearing volatiles to mobilize from the relatively warmer EFS regolith and/or be sequestered towards the relatively colder PFS regolith (Vasavada et al., 1999; Siegler et al., 2011).

Fig. 1a and b illustrates the pattern characteristics of slope hydration and inferred temperature on the slopes of a Martian crater, depicting a deposit of water-frost in winter (blue) as observed by the 3- μm band of the Mars Compact Reconnaissance Imaging Spectrometer onboard the Mars Reconnaissance Orbiter. Fig. 1a depicts the location of the blue crescent-shaped water-frost deposit on the crater's inner slopes that correspond to the craters minimum incident solar irradiation, while surfaces that receive direct solar irradiation are relatively anhydrous (grey). Fig. 1b illustrates the detection of such a deposit with a hypothetical neutron (green circle) and temperature sensing instruments. The slope azimuth angle Φ , defines the angular deviation of the slope aspect relative to the pole-facing direction. In the most pole-facing slope position $\Phi = 0$, the water concentration detection is the greatest where the deposit is spatially the broadest, as indicated by the maximum suppression in the neutron count rate. The hydrogen concentrations decrease with increasing slope azimuth angle towards EFS. At the terminus of the hydrated zone and continuing towards EFS conditions the epithermal count rates have no slope, thereby indicating uniformly anhydrous conditions relative to PFS. In comparison, the temperature rates have a continuously

positive gradient between PFS and EFS (red) due to a correlated increase in insolation. Importantly, the local surface hydrogen concentrations, temperature and illumination rates are maximally contrasted by comparing the respective rates on PFS and EFS.

If there exists a global-scale and active production of hydrogen at the surface as described in Sunshine et al. (2009), then the detection of hydrogen-bearing deposits by orbital neutron remote sensing is influenced by the spatial scale of the deposits. Possibly meter-scale hydrogen-bearing deposits on PFS may at least temporarily, be supported by the combined effects of low solar incidence angles and low regolith thermal conductivity $\sim 1.5 \times 10^{-5} \text{ W/cm}^2 \text{ K}$ in the upper-latitudes (Keihm et al., 1973). Meter-scale deposits are far below the spatial resolution of orbital neutron remote sensing methods so the detection of hydrogenous materials by orbital neutron methods should be dependent on the spatial scale of hydrated spots. Orbital neutron remote sensing is inherently a convolution process related to the repeated observation of a given region and the integration of detected neutrons into a count rate map. An epithermal detector's differential instrument response to any locally hydrated or anhydrous spot is then a function of (1) the magnitude of the hydrogen concentration contrast between the spot and the surrounding area and (2) the spot area relative to the area of the instrument footprint, as defined by the surface area subtended by the instrument field-of-view. In Fig. 1b (blue-dashed) we illustrate the diminished detection of a hydrated spot that is spatially smaller in scale. If the hydrated spot is smaller or the detector altitude higher, then by averaging within the instrument footprint, the hydrated spot will become less detectable as a function of the decrease in the ratio of the hydrated spot area to the footprint area, thus causing a decrease in the magnitude of epithermal suppression. In Fig. 1b this effect is illustrated as a corresponding decrease in the detected hydrogen concentration at the PFS position. Similarly, the epithermal rate suppression and magnitude of the hydrogen detection increases for larger spot areas until the areas are equal. Further, the hypothesis implies there is no epithermal contrast for anhydrous spots towards EFS that are hydrated to levels similar to those of surrounding regions. It is also important to note that the temperature sensor response to slope scale will be fundamentally different than the epithermal sensor response. Its response to smaller scale topography will be similarly blurred by the sensor, but be indicated by the lowering of the plot gradient Fig. 1b (red-dashed), thus diminishing PFS rates and enhancing EFS rates. For further discussion see Section 4.2 and the Supplemental on-line materials.

Neutron remote-sensing techniques have a well-established heritage in hydrogen volatile studies of the inner planets and small

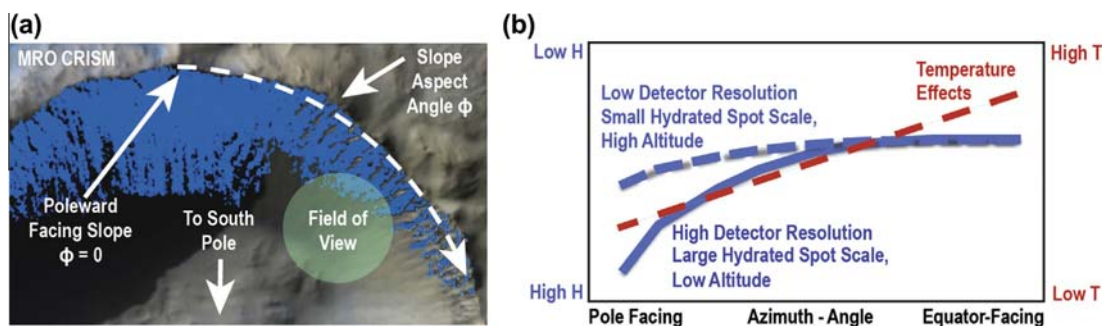


Fig. 1. Crater slope hydration depending on slope azimuth angle and illumination in a martian crater, from Vincendon et al. (2010). (a) Winter water frosts (blue) on the inner slopes of a southern hemisphere crater by the 3- μm band of the Mars Compact Reconnaissance Imaging Spectrometer onboard the Mars Reconnaissance Orbiter. The crescent shaped water deposit illustrates the water deposit shape, position and symmetry with respect to the craters inner pole-facing slopes. The green circle illustrates the hypothetical field-of-view of a neutron detection instrument. (b) Hypothetical hydrogen and temperature plots observed over the crater in (a) by an epithermal neutron detector (solid blue) and a radiometer (temperature) sensor (red) as a function of slope aspect angle. Epithermal neutron flux suppression due to hydrogen is maximum on pole-facing slopes and diminishes towards equator-facing slopes. In comparison, temperature increases continuously between pole and equator-facing slopes due to insolation.

bodies (Feldman et al., 1998; Boynton et al., 2004; Litvak et al., 2008; Mitrofanov et al., 2010a, 2010b; Prettyman et al., 2011; Lawrence et al., 2011). Neutrons are created by galactic cosmic-ray interactions with regolith nuclei and some neutrons are lost to space as a detectable leakage flux. The leakage flux of epithermal or medium energy neutrons, $0.4 \text{ eV} < E < 10 \text{ keV}$ is especially sensitive to hydrogen and is largely insensitive to temperature, unlike the thermal emission and photometric effects that conditionally degrade the interpretation of NIR and FUV measurements (Feldman et al., 1993; Little et al., 2003; Paige et al., 2010a, 2010b; Clark et al., 2011; McCord et al., 2011). These factors make epithermal neutrons ideally suited for the study of hydrogen volatiles at the Moon's poles.

LEND's design includes eight ^3He detectors and a scintillator to measure the fluxes of thermal, epithermal, and fast neutrons (Mitrofanov et al., 2010a, 2010b). For this research epithermal neutron observations from LEND's collimated CSETN instrument are mapped to determine the Moon's surface concentrations and spatial distributions of hydrogen at up to a meter in depth. The CSETN instrument design includes a passive neutron absorbing collimator containing ^{10}B and polyethylene. This collimator permits surface emissions of epithermal neutrons to freely enter the CSETN detectors within a $\pm 5.6^\circ$ angle about the instrument bore-site. From the nominal 50-km mapping altitude, this configuration yields an instrument field-of-view (FOV) nadir view of the surface that provides a $\sim 10 \text{ km}$ FWHM (Full-Width Half-Maximum) surface resolution (Mitrofanov et al., 2010b). To increase the signal-to-noise ratio, four identical co-aligned epithermal neutron detectors are located within the collimator, thus defining the collimated field-of-view and a factor-of-four increase in the integrated signal rate as compared to a single detector. The detailed procedure to convert maps of neutron count rates to $\text{H}/\text{H}_2\text{O}$ concentrations is described in Mitrofanov et al. (2008) and Mitrofanov et al. (2010b). Detailed procedures for the calibration and processing of the LEND data are described in Mitrofanov et al. (2012), Boynton et al. (2012), and Litvak et al. (2012a, 2012b).

3. Data reduction and methods

Fig. 2a–d illustrates south-polar stereographic maps between S and S latitude derived from LRO instrumentation used in this study. Fig. 2a shows the CSETN epithermal neutron count rate map with permanently shadowed areas outlined in white, the map includes observations obtained between July 2, 2009 and November 6, 2013. Fig. 2b shows the LOLA altimetry measurements as a digital elevation model (DEM) of the lunar surface. That map is the basis map for the derivation of topographic slope and slope azimuth angle maps, as well as illumination model maps (Smith et al., 2010; Mazarico et al., 2011). Fig. 2c shows the LOLA Average Visible Illumination model (LAVI) derived from the modeling of illumination as a function of topography, lunar and solar ephemeris. The LAVI map represents a normalized percentage of the number of times any fraction of the solar disk is visible as evaluated over several lunar precessions. Fig. 2d shows the Diviner map of the average south polar temperatures derived from the bolometric brightness of the surface emission of infrared radiation in wavelengths between 0.3 and 400 μm (Paige et al., 2010a, 2010b). A decomposition of the epithermal, illumination and temperature maps in Section 4.1 is constrained to the high-latitude region, 80–90°S defined by the latitude domain of the publicly available Diviner polar resource products. Map sources for these data products are available at the National Aeronautics and Space Administration's (NASA) Planetary Data System (PDS). Mapping and analytical methods are further described in the [Supplemental on-line materials](#).

All maps were identically produced or registered to a common 1-km² pixel resolution that is a significantly higher resolution than the nominal CSETN footprint resolution, but facilitates the study of the influence of the spatial scale of slopes on CSETN signal rates. Mapping for CSETN was performed using its fully-calibrated 1 Hz observations. At times during the CSETN mission the number of active detectors has varied, so for the full-mission mapping the integral counts in each observation are scaled to the rate of a four detector system.

The CSETN full-mission map convolves a ~ 4.5 year average of surface solar irradiation and temperature conditions. Over such long periods, direct solar irradiation I to the surface has varied as a diurnal function of the average insolation, $I = F \cos \Omega$ (Ritter and Kochev, 2002). Where F is the solar constant at one astronomical unit and the angle Ω describes the map of time-averaged solar incidence angles with respect to the topography surface normal and contains the combined effects of latitude, topographic slope and slope aspect. We assume that the volatilization of hydrogen-bearing materials in the lunar regolith is a function of insolation. As a result of the long term averaging, the combined angular effects in Ω are reduced. The Moon's small seasonal axial tilt ($< 1.5^\circ$) provides an additional constraint on local insolation variation and establishes a maximum insolation direction that is assumed along each map pixels meridian. PFS and EFS are then defined as the topographic end-members for insolation conditions. Fig. 3 illustrates the components of topographic slope θ (left) high slope is bright. Slope azimuth angle Φ (right) is illustrated, where the contrasting dark regions correspond to PFS, white regions correspond to EFS and (grey) regions correspond to both east and west-facing slope conditions. Slope azimuth angle has a range between 0° and 180° , whose bounds define PFS and EFS conditions, respectively.

Maps within the 80–90°S latitude band were averaged as a function of slope and slope azimuth angle in bins of 1° of slope and 10° of slope azimuth angle called “insolation grids”, Fig. 4 (left column) (McClanahan et al., 2013). Pixels from slopes of $> 20^\circ$ have small aerial contributions and are included in that band. Importantly, this bulk averaging technique yields a scale-invariant transformation of the topography that is independent of spatial scale as respective rates from all crater slopes are uniformly mapped into the full range of slope azimuth angle.

4. Results

4.1. Insolation and the hydration of pole-facing slopes

Fig. 4 illustrates strong evidence that hydrogen concentrations on PFS are locally enhanced as indicated by the highly correlated, low epithermal, illumination and temperature rates corresponding to the upper-sloped PFS conditions of the insolation grids (left column). Fig. 4a illustrates the CSETN grid. Fig. 4c illustrates the LAVI grid. Fig. 4e illustrates the Diviner grid. Corresponding plots of the insolation grids averaged into three slope-bands illustrate the suggested enhancement in hydrogen concentrations towards PFS, Fig. 4b, d, and f (right column) as respective averages of low-slope ($\leq 6^\circ$), medium-sloped ($> 6^\circ$ to $< 13^\circ$) and highly-sloped ($> 13^\circ$) conditions. In all three of the plot figures, the corresponding rates on PFS are minimized. For CSETN, the slope azimuth angle rates in the PFS low, medium and highly sloped position are [0.1%, -0.6% , -1.3%] of the lunar induced epithermal rate relative to the -45° to -90° latitude band, respectively. Positive plot gradients for all three datasets indicate the correlation of epithermal rates to the Fig. 1 depiction of regolith conditions that are increasingly anhydrous towards EFS. Similarly increasing average illumination and temperature rates are well correlated with the epithermal rate trends.

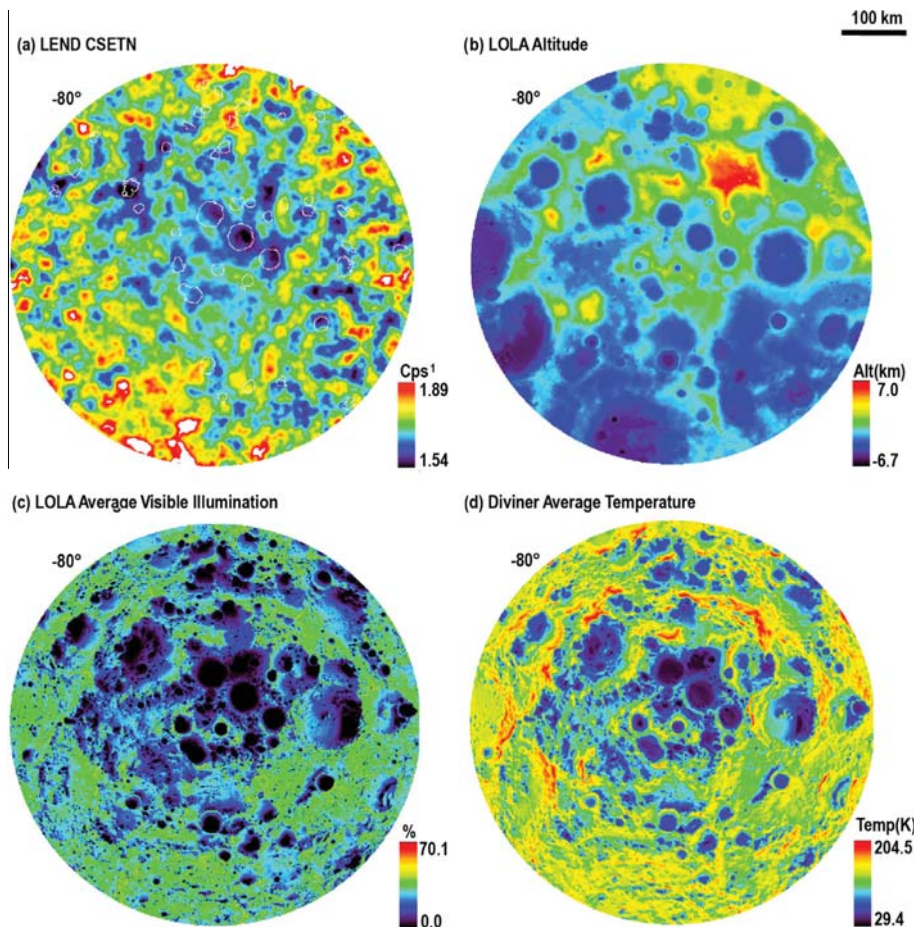


Fig. 2. South polar stereographic maps 80–90°S from Lunar Reconnaissance Orbiter instrumentation. (a) Lunar Exploration Neutron Detector (LEND) Collimated Sensor for Epithermal Neutrons (CSETN), units in spacecraft background corrected counts-per-second (cps) relative to a 1.7 cps collimated rate¹ with outlines of permanently shadowed regions (*white*). CSETN map includes fully calibrated observations made between July 2009 to November 2013. (b) LOLA Altitude, units are in units of km deviation from the mean 1737.4 km lunar radius. (c) LOLA Average Visible Illumination (LAVI) as the normalized percentage of the time any portion of the solar disk is observed. (d) Diviner average surface temperature in degrees Kelvin. CSETN was additionally smoothed for this visualization using a 10 km wide (3.6 km FWHM) Gaussian kernel.

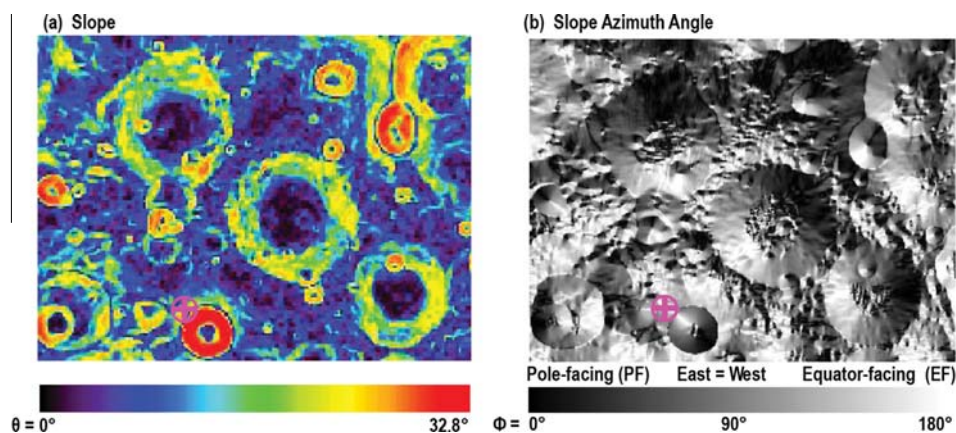


Fig. 3. Maps of south polar topographic slope and slope azimuth angle used to classify and segment the epithermal neutron, illumination and temperature maps. (a) Slope θ is in degrees of inclination from the local horizontal plane. (b) Slope azimuth angle ϕ defines the slope aspect's angular deviation in degrees from the pole-facing direction. Slope azimuth angle ranges from pole-facing $\phi = 0$ (*black*) to equator-facing directions $\phi = 180$ (*white*). The south pole is at the *pink*+. Epithermal, illumination and temperature map pixels are averaged as a function of slope and slope azimuth angle.

Evidence from the insolation grid plots indicate the EFS epithermal neutron leakage flux is slightly anti-correlated with slope degree in a comparison with the corresponding Diviner temperature plots, Fig. 4a, b, e and f. Isotropic galactic cosmic rays (GCR) generate the surface neutron leakage flux. Surfaces of increased

slope have a decreasing solid angle to sky and thus should indicate a commensurate reduction in GCR influx and neutron leakage flux. Approaching 20° of slope, the solid angle to sky should be decreased by a minimum of ~11% as compared to a no slope surface that has a 2π steradian solid angle to sky. CSETN rates are

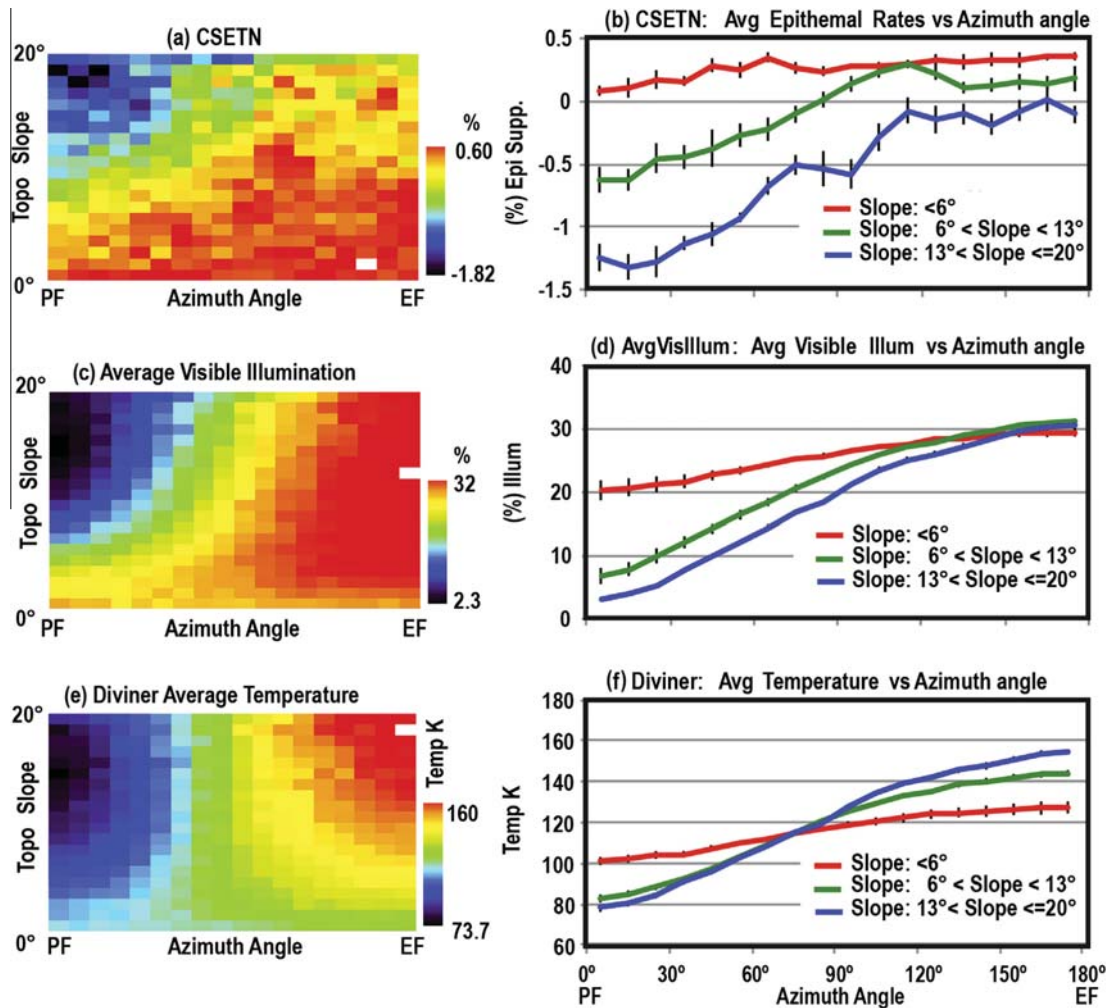


Fig. 4. South polar insolation grids and averaged plots of epithermal neutron, temperature and illumination rates as a function of slope and slope azimuth angle. (left column) Insolation grids include (a) Collimated Sensor for Epithermal Neutrons (CSETN), (c) LOLA Average Visible Illumination (LAVI) and (e) Diviner average temperature maps. Insolation grids were derived using the topography between 80°S and 90°S. (right column) Corresponding plots show the respective insolation grids averaged into three slope bands (red: 0–6°, green: 6–13°, blue: >13°). PF = Pole-facing, EF = Equator-facing. The length of the error bars are in units of twice the standard-error of the mean as determined in the slope bins corresponding to each plot.

observed to be largely independent of slope degree on EFS, but towards the upper EFS, the epithermal neutron count rate suppression is decreased $\sim 0.35\%$ relative to the average low-slope EFS rate. However, the decrease in the neutron leakage flux should be a symmetric function for the full range of slope azimuth angles. Any slope dependent decrease of GCR on the total PFS neutron leakage flux can then only be considered a partial contribution approaching 25% of the total PFS suppression at 20° of slope, thus the estimates of PFS hydrogen concentration may be decreased. A correction for this factor is not included in this research, but will be considered in a future study.

An upper-bound for the illumination and temperature rates that can entrain hydrogen on slopes is suggested by the CSETN high-slope plot, Fig. 4b. As compared with the epithermal rate plot in Fig. 1b, where the slope azimuth angle approaches anhydrous conditions, the epithermal neutron rate gradient approaches no slope. A break in the highly sloped CSETN plot gradient suggests the upper-bound conditions for near surface hydration are observed at the position where the azimuth angle = 110°. That position corresponds to an upper-limit temperature of 135 K and the LAVI rate = 25%. The result is consistent with upper-bound temperature estimates found by Schorghofer and Taylor (2007).

Fig. 5a and b illustrates scattergrams of the CSETN vs. the LAVI (left) and the CSETN vs. the Diviner temperature (right) insolation grids. Pearson correlation = [0.83, 0.56], respectively. To illustrate any rate dependence on slope, the insolation grids were, similar to the analysis in Fig. 4, split into three bands: low slope: 0–6°; medium 7–12°; high: >13°. All the insolation grids show an enhanced suppression of rates towards the upper-sloped PFS. A linear fit of each slope band shows the slope dependent increase in suppression level. Pearson correlation of the PFS and EFS halves of the insolation grids illustrate the contrasting correspondence of the CSETN rates to the LAVI and Diviner grids, CSETN vs. LAVI = [0.88, 0.66] and CSETN vs. Diviner [0.44, –0.40], respectively. The correlation difference may be explained in the method by which the LAVI model algorithm counts solar irradiation to the lunar surface. Diviner temperatures are maximized towards highly-sloped, EFS conditions by the cosine of the combined angular effects of insolation, Fig. 4f. In contrast, the LAVI algorithm produces a map of the normalized count of the number of times any part of the solar disk is in the view of each pixel, as measured by a simulation of the ephemeris over several lunar precessions. In the high-latitudes, most PFS pixels are in or near permanent shadow. Proceeding in slope azimuth angle from PFS to EFS, some

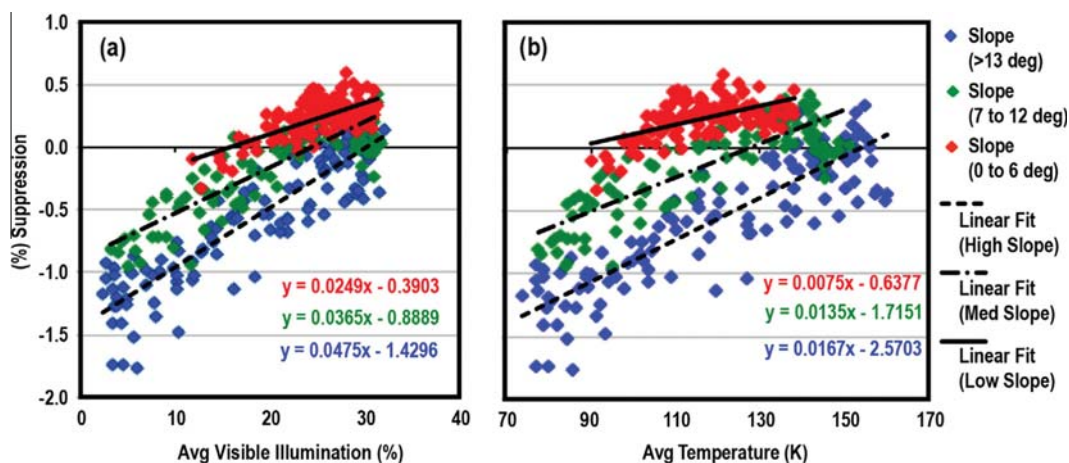


Fig. 5. Scattergrams of the correlated insolation grids for the epithermal neutron rates vs. the average temperature and average illumination. (a) Correlation of the Collimated Sensor for Epithermal Neutrons (CSETN) with the LOLA Average Visible Illumination (LAVI) Fig. 4 grids. (b) CSETN correlated with the Diviner Radiometer Fig. 4 grids. Each correlation was decomposed into three slope specific bands, low slope ($\leq 6^\circ$) red, medium slope ($>6^\circ$ and $\leq 13^\circ$) green, and high slope ($>13^\circ$) blue. Linear fits of the slope band correlations illustrate the increasingly enhanced suppression of epithermal neutron count rates towards upper-sloped, pole-facing conditions.

fraction of the solar disk is observed in increasing frequency, but closer to EFS that frequency becomes uniform, as indicated by the diminished plot gradients, Fig. 4d. In comparison, the CSETN trend suggests hydrated conditions towards PFS that become increasingly and then uniformly anhydrous towards EFS, Fig. 4b. These results appear to limit the possibility that volatile hydrogen concentrations may persist for long durations towards EFS conditions, except possibly in high-latitude, low illumination conditions e.g. ~permanent shadow or within voids in regions of high surface roughness.

Plot evidence clearly illustrates that the EFS rates in the CSETN and LAVI insolation grids are not well correlated with corresponding Diviner temperatures, Fig. 4b, d and f. The result indicates that on EFS the epithermal neutron leakage flux and LAVI rates are not slope dependent but temperature is. Theoretical studies have shown that the energy of thermal neutrons <0.4 eV can be enhanced by temperature into detectable epithermal energy ranges >0.4 eV (Little et al., 2003; Feldman et al., 2001). Based on those results the LPNS calibration processing included a small latitude specific correction for temperature in its standard data processing (Maurice et al., 2004). The implications for this research are that the PFS to EFS temperature contrast could explain the observed epithermal neutron flux contrast. If the epithermal rates do vary with temperature, then the CSETN EFS rates should increase with the corresponding Diviner rates with increased slope. Instead, the CSETN and Diviner EFS rates are slightly anti-correlated. An observed EFS range of 43 K is derived from the south polar Diviner temperature grid, 117 K at 0° of slope and 160 K at 20° . It is also possible that the observed slope-dependent decrease in CSETN EFS rates due to GCR effects may offset any temperature effect. If so, then any temperature contribution to the CSETN PFS to EFS contrast must be much less than the observed contrast. However, the study is limited to the top 10° of latitude and the range of EFS temperatures indicated. These results may differ in the mid-latitudes where temperatures are considerably higher. In summary, the lack of correlation between the CSETN and Diviner EFS rates suggests that the contrasting PFS to EFS temperatures do not explain the corresponding epithermal rate contrast, nor does it suggest that in the observed temperature range a correction is warranted.

Fig. 4 results also indicate evidence that the PFS are being hydrated globally and in a continuum of spatial scales as observed by the localization of the suppression minima towards the CSETN upper-sloped ($\geq 13^\circ$) PFS insolation grid bins, Fig. 4a. Fig. 2 map slope distributions averaged in the insolation grids generally

follow a power-law distribution from low to high-slope. Highly sloped conditions constitute only 22% of the surface area in the southern polar cap between 80°S and 90°S latitude (Rosenburg et al., 2011). Analysis suggests that the low-slope pixels are more likely to be a part of smaller-scale and less detectable topographic features. Epithermal neutrons from smaller topographic features are blurred as a function of their diminished areal contributions to the CSETN instrument field-of-view, thus resulting in the lower PFS to EFS contrast as observed in the low-slope $<6^\circ$ plot, Fig. 4b. The greater contrast observed on the highly sloped plot is then attributable to the increase in the signal-to-noise ratio produced by the sampling of larger-scale slopes. PFS pixels on larger-scale slopes are more detectable by the support of pixel neighbors that are also highly sloped and have similar slope azimuth angles. A second factor influencing the diminished low-slope epithermal rate gradient is that the illumination or temperature of low-slope pixels may not be definitive as low slope pixels can be in permanent shadow or illuminated. Highly sloped insolation bins are less likely to have averaged pixels with differing illumination and temperature characteristics.

4.2. The magnitude and latitude extent of pole-facing slope hydration

To quantify the magnitude and latitude extent of the epithermal neutron flux contrast between PFS and EFS, an analysis window, 10° wide in latitude and divided by the azimuthal plane was used to determine EFS and PFS latitude rate profiles. The analysis window was systematically shifted in 0.5° increments from the west ($180\text{--}360^\circ\text{E}$) longitudes, through the south pole, to the east longitudes ($0\text{--}180^\circ\text{E}$), beginning and ending at 50°S latitude. Similar methods have been used to determine latitude-band averages of the Moon's epithermal neutron flux, defined as orbital phase profiles (Feldman et al., 1998; Litvak et al., 2012). At the center latitude position of the window, the averaged PFS and EFS epithermal neutron flux is defined. Over the series of window latitude positions the independent PFS and EFS rate profiles are derived. Note that topographic slope is not a factor in this analysis.

4.2.1. Slope hydration detection and the dependence on spatial scale

A second part of the experiment in 4.2 is to determine if the detection of epithermal neutron flux is dependent on slope spatial scale. Pixel neighborhoods in topography that have highly variant slope azimuth angle distributions are a signature of smaller-scale surface features as determined by their comparatively greater rate

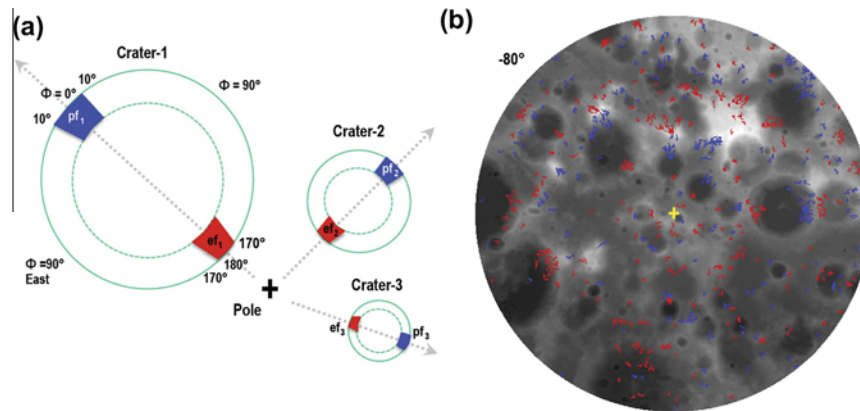


Fig. 6. (a) The segmentation of equator-facing and pole-facing spots as a function of spatial scale. Equator-facing, $\Phi > 170^\circ$ (red) and pole-facing angle, $\Phi < 10^\circ$ (blue) slope pixels are isolated as a function of their slope azimuth angle. Small-scale slopes $i = 3$, have a greater rate of change in their azimuth-angle neighborhoods than *Large*-scale slopes depicted by three idealized craters, $i = [1, 2, 3]$. (b) The set of south polar 80–90°S *Large*-scale >15 km² equator-facing (red) and pole-facing spots (blue).

of change for small features, Fig. 6a, crater #3. Conversely, pixel neighborhoods with less variant slope azimuth angle distributions are a signature of larger-scale slopes and a more coherent and detectable surface by its larger cross-section with the instrument field-of-view. e.g. Fig. 6a, crater #1. To isolate the epithermal neutron count rates observed from larger-scale slopes, pixel clusters were aggregated in the topography as a function of their slope azimuth angle. A pixel region-growing process was performed to aggregate contiguous pixels into independent distributions of EFS $\Phi < 10^\circ$ and PFS $> 170^\circ$ “spots”, whose areas were determined. Region growing is an image segmentation technique that classifies and aggregates contiguous pixel neighborhoods as a single entity, subject to predetermined rules, that for this study is slope azimuth angle in EFS or PFS classifications (Sonka et al., 1996). By applying a lower-bound discriminator to the distributions of spot areas, spatially large-scale EFS and PFS spots with low slope azimuth angle variation were segmented. Two spatial scale conditions were evaluated (1) *All*: where pixel clusters are greater than or equal to 1 pixel = 1 km², i.e. no-filter; and (2) *Large*: (>15 km²) pixel clusters with aggregate areas greater than 15 km². The spot aerial threshold of 15 km² was established via pilot study. The LAVI map was processed in parallel with the CSETN analysis using the available 65–90°S latitude. Fig. 6 illustrates the method as well as the *Large*-scale PFS and EFS spot distributions.

Several properties of the *Large*-scale pixel distributions indicate that the spatial scale of the slopes was increased in the segmentation. The LAVI PFS illumination rate decreased between 3% and 5% as compared to the *All* case, Fig. 7a. Also, the average slope of pixels in the *Large*-scale distributions increased 3.5% from the *All* slope average $\sim 7^\circ$, to *Large* 10.5°. Other evidence that the spots in the *Large*-scale distributions are of increased scale was obtained by convolving a 3×3 pixel neighborhood kernel through the slope azimuth angle map. It was found that the average standard deviation of the slope azimuth angle for *Large*-scale pixel distributions, $14.5 \pm 16.1^\circ$ was lowered by nearly a factor of two as compared to the average for the *All* distributions, $26.1 \pm 19.1^\circ$.

The magnitude and latitude extent of the EFS and PFS rate contrasts derived from the LAVI and CSETN maps are illustrated in Fig. 7. EFS and PFS results for the *All* study are illustrated in green and light-blue, respectively. Correlated LAVI rates show the symmetric suppression of PFS and EFS illumination rates that correspond to the decrease in the solar incidence angle and the greater levels of shadowing. EFS illumination rates for the *All* condition are latitude dependent and higher than the respective PFS rates in the entire 65–90°S region. Approaching the poles, the gradient of the LAVI EFS rate profile is lower and less variant than the PFS profile, thus emulating the EFS epithermal neutron rate trend for anhydrous surface conditions described in Section 4.1.

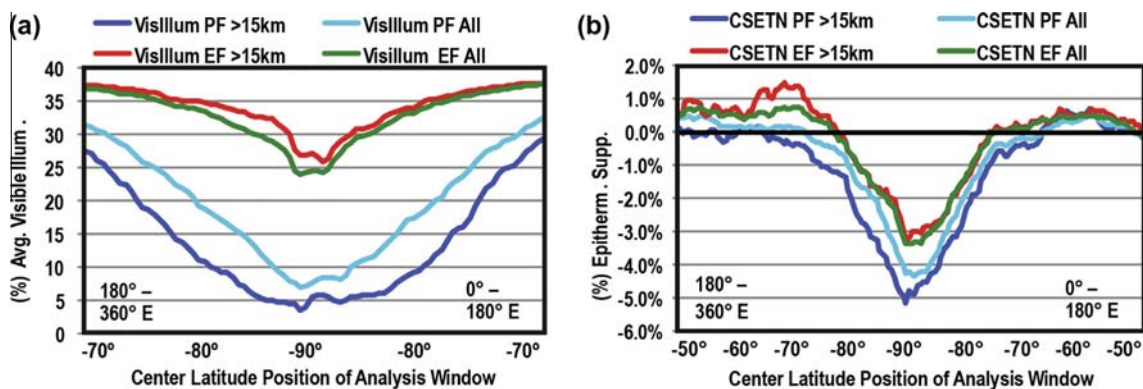


Fig. 7. Latitude profiles of the LOLA Average Visible Illumination and CSETN epithermal neutron rates for equator-facing and pole-facing slopes. Averaged equator-facing and pole-facing rates were derived within a sliding 10°-wide analysis window. (a) The available LAVI map was correlated to topography between 65°S and 90°S and (b) CSETN correlation was analyzed between 45°S and 90°S latitude. *All* results show the averages of both LAVI and epithermal neutron rates for all pole-facing (light blue) and equator-facing pixels (green). The average bias in hydrogen concentration of ~ 23 ppmw hydrogen is indicated by the $\sim 1\%$ contrast in the epithermal rates on poleward and equator-facing slopes. The polar epithermal neutron flux contrast is enhanced to $>2\%$ for *Large*-scale slopes, >45 ppm. The contrast enhancement is attributable to the increased signal-to-noise and detectability of *Large* pole-facing slopes, suggesting a widespread hydration effect.

The baseline CSETN PFS and EFS profiles show the broad polar suppression of latitude averaged epithermal neutron rates found by Feldman et al. (1998) and Litvak et al. (2012). The maximum suppression in the baseline profiles at the pole are EFS: $3.3 \pm 0.04\%$ and PFS: $4.3 \pm 0.03\%$ relative to the average epithermal rate in the 45–90°S latitude band. Importantly, the contrast in EFS and PFS epithermal latitude rate profiles is greatest near the poles and decreases towards the mid-latitudes. At the pole the *All* contrast (EFS – PFS) is maximized at $\sim 1\%$ of the lunar induced epithermal rate and is consistent with an interpretation of a ~ 23 parts-per-million-by weight (ppmw) H bias towards PFS within the upper-meter of regolith. The latitude bands at which the profile contrast begins is in the west longitudes near -50°S and east longitudes near 65°S . The result suggests that in mid-latitudes below these positions the detection of hydrogen by CSETN is negligible and that PFS hydration of the surface increases poleward of these latitudes.

An increase in both the PFS specific signal-to-noise and the inferred detection of hydrogen is indicated for most of the upper latitudes. That result is indicated by the enhanced suppression of epithermal rates in the PFS *Large* result as compared to its respective *All* case. At the pole, the maximum suppression is increased to $5.2 \pm 0.12\%$ and the magnitude of the polar contrast (EFS-PFS) doubles to $2.0 \pm 0.17\%$ or ~ 45 ppm hydrogen, though an observation of $\sim 2.4\%$ is indicated at 87°W . Importantly, the latitude extent of the *Large*-scale epithermal contrast is enhanced towards the mid-latitudes to 50°S W longitudes and remains at 65°S in the E longitudes. Both the magnitude and latitude extent of the *Large*-scale contrasts are increased relative to the *All* study and approach the latitude extent of south polar hydration, -40° observed by NIR measurements (McCord et al., 2011).

The *Large* CSETN EFS suppression at the south pole remained statistically unchanged at $3.2 \pm 0.12\%$ as compared to its respective *All* study. That lack of contrast over most of the Moon's southern polar region further substantiates the hypothesis that the hydration on EFS slopes is equivalent to surrounding regions as indicated by the invariant CSETN EFS rates depicted in Fig. 4a. However, a notable exception does occur near 70°S W longitude, where the EFS *All* profile (*green*) is slightly lower, $\sim 0.5\%$ than its respective *Large* (*red*) profile over the analysis span of $\sim 10^\circ$ in latitude. The result may indicate the increased statistical uncertainties inherent in the PFS and EFS spot distributions towards lower latitudes or possibly contrasts induced by temperature or space weathering effects. Note that similar EFS contrast differences are observed

for the mid-latitude results of LPNS and SETN that are illustrated in the Supplemental on-line materials.

To put the EFS vs. PFS epithermal neutron contrasts into perspective, a 1% contrast explains about one fourth of the $\sim 4\%$ total polar suppression of epithermal neutron flux identified by LPNS and LEND in the latitude-band averages observed by Feldman et al. (1998) and Litvak et al. (2012). In considering the *Large*-scale study, the observed $\sim 2\%$ epithermal rate contrast explains nearly half of the total south polar epithermal flux suppression. The remainder of the epithermal suppression is likely explained by the instrumental blurring of hydrated spots in small-scale topography that are well below the resolution of the CSETN detector. The EFS evidence depicted in Fig. 7a and b suggests no polar suppression would be observed on EFS if given an ideal, infinitely high-resolution detector and only first order topography and illumination conditions akin to the dimpling on a golf ball. The entirety of the observed polar suppression of epithermal rates would then be attributable to hydrogen distributions that are concentrated around PFS, similar to the surface hydrogen deposit illustrated on the PFS slopes of Fig. 1a.

In Fig. 8a and b the LAVI and CSETN contrasts for the EFS and PFS profiles illustrate the latitude extent and latitude variation in the contrast magnitude for the two spatial scale studies. Contrasts are determined as the difference between EFS and PFS profiles (EFS-PFS) in each study. The maximum epithermal contrast in the baseline study *All* (*black*) profile is, $\sim 1.06 \pm 0.06\%$ at 87°S W longitude. The difference is measured as the difference in EFS and PFS pixel distribution means. Uncertainties are defined in quadrature from the standard error of the means of the EFS and PFS pixel distributions. Uncertainty units are stated in a 1-sigma quantity. Towards lower latitudes, the contrast in epithermal rates decreases, suggesting a decrease in the level of PFS hydration. However, the trend of the epithermal rate contrast towards lower latitudes in the W and E conditions is slightly \sim asymmetric, as indicated by the slightly greater contrast in the W longitudes. The *Large*-scale contrast plot (*green*) indicates that the maximum contrast is $\sim 2.4 \pm 0.17\%$ in the window position at 87°S W longitude. The polar contrasts similarly decrease with lower latitudes. Epithermal contrast averages for each hemisphere were (1) *All* East = $0.35 \pm 0.3\%$; West = $0.52 \pm 0.2\%$ and (2) *Large*: East = $0.59 \pm 0.5\%$; West = $1.3 \pm 0.5\%$. The contrast asymmetry illustrated in Fig. 8b, may be explained by a small, but noticeable difference in the illumination rate contrast in comparing W and E

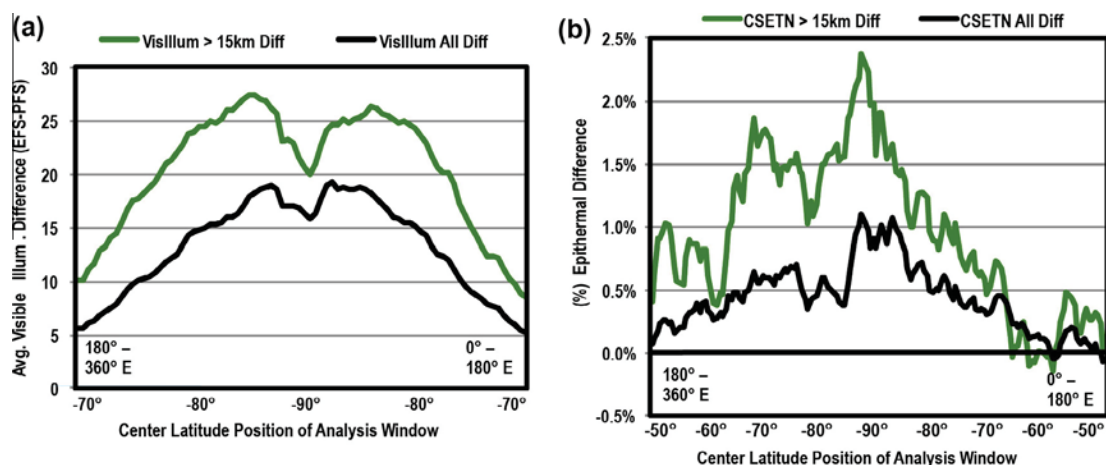


Fig. 8. LOLA Average Visible Illumination (a) and Collimated Sensor for Epithermal Neutron (CSETN), (b) epithermal count-rate contrasts (EFS-PFS) for *All* and *Large* cases in Fig. 7. Average Visible Illumination and epithermal rate contrasts show correlated trends that have maximized contrasts at the poles and decrease towards the mid-latitudes. Scale dependent contrast increases for the *Large* study are primarily due to the increased suppression of rates on pole-facing slopes. Maximum polar contrasts for the two spatial scale studies were *All* $\sim 1.06 \pm 0.06\%$ and *Large* $2.4 \pm 0.17\%$ respectively.

longitudes in Fig. 8a. Another possible explanation comes from studies by Clark et al. (2011), and McCord et al. (2011). Those studies suggest that the surface variation in hydroxyl concentrations is governed by the more limited availability of oxygen in the regolith of basaltic mare as compared to highland terrain. McClanahan et al. (2012), similarly found the EFS and PFS epithermal rates in the two hemispheres to be ~asymmetric in a correlated study of the LEND Sensor for Epithermal Neutrons (SETN) and LPNS, reviewed in the [Supplemental on-line materials](#).

The diminishing EFS vs. PFS epithermal rate contrast towards the mid-latitudes offers a second line of evidence that the temperature contrast on PFS and EFS does not explain the observed epithermal rate contrasts. An examination of the slope distributions shows that *Large-scale* slopes do exist in the mid-latitudes though the corresponding temperatures are not evaluated here. Those slopes should provide an equivalent temperature contrast that is evidenced by proxy using the illumination rates in Fig. 7a. Mid-latitude temperature ranges on PFS and EFS differ from polar latitudes. Yet the epithermal contrasts diminish towards the mid-latitudes, suggesting there is a poleward decrease in the level of slope hydration towards PFS. A second possible factor to consider in these results is detector altitude, which has varied during the circular and elliptical mission segments and shows higher average altitudes over the mid-latitudes. Independent analysis of the LEND CSETN circular orbit mission data show similarly diminished epithermal contrasts in the mid-latitudes.

Another potential explanation for the epithermal contrasts is that EFS and PFS slopes are diurnally exposed to very different temperature distributions that may lead to asymmetric space weathering, optical maturity or mass wasting effects that could influence epithermal rates (Lucey et al., 2014; Lawrence et al., 2014). Such a geochemical or geophysical alteration of the regolith identified here specific to PFS, would then have to at least partially cause the relative suppression of epithermal flux on PFS and also be latitude dependent, and maximized at the poles thus emulating the effects of locally enhanced hydrogen concentrations towards PFS.

Strong support of the PFS hydration hypothesis is made by the finding of a statistically significant contrast in epithermal count rates in the EFS and PFS spot distributions. A statistical *t*-test of the respective EFS and PFS spot distribution means was performed using the latitude-band poleward of 65°S. In this region, the average PFS epithermal count rate suppression is greater than the respective EFS rates for all latitudes. For the *All* case, PFS: 28908 and EFS: 30073 spatially independent spots greater than or equal to one pixel were identified and the difference in class distribution means was determined to be significant at the 6.5 σ level. For the *Large* case: 831 and 916 spatially independent PFS and EFS spots were classified in the same latitude band and the difference in class distribution means was significant at the 4.8 σ level.

The uniqueness of the observed PFS vs. EFS contrasts and quality of the map registration was evaluated by systematically rotating the CSETN and LPNS epithermal neutron count rate maps against the topography. Each map was rotated in 360, 1° increments using the latitude band between 65°S and 90°S latitude (McClanahan et al., 2012). At each map orientation the difference (EFS-PFS) in average epithermal neutron count rates was measured for the EFS and PFS spot distributions, partially depicted in Fig. 6b. For both CSETN and LPNS the average contrast between PFS and EFS rates was found to be maximized at the position where the CSETN and LPNS maps were fully-registered with the topography.

Finally, an identical analysis of the LEND SETN and LPNS epithermal neutron maps was performed as described in Section 4. Those results broadly support the conclusions of this paper and are reviewed in the [Supplemental on-line materials](#).

5. Discussion

Solar wind interactions with regolith silicates may actively produce loosely bound hydrogen volatiles that migrate laterally or through the surface and get trapped in the locally stable trapping conditions in PFS (Zellar et al., 1966; Crider and Vondrak, 2000; Schorghofer and Taylor, 2007). Fig. 8 illustrates evidence for an isotropic source of hydrogen reflected in the nearly symmetric epithermal neutron flux contrasts that diminish away from the poles. Hibbitts et al. (2011) considered the residence time of water molecules on lunar grains using temperature-programmed desorption measurements and found temperature dependent residence times of 10² s at 200 K and 10⁶ s at 160 K. Analysis of the insolation grids with Fig. 4 CSETN and Diviner averaged rates indicate that hydrogen volatiles may have significantly longer residence times on high-latitude PFS where the temperature range was found to be 74–109 K as compared to the 117–160 K temperature range on EFS. Areas of low to no illumination conditions on PFS increase in area with higher-latitudes as shadows elongate to mostly span craters in the high-latitudes, thus providing greater areas for hydrogen to become entrained, as illustrated in Fig. 1. A latitude dependent increase in the level of topographically induced shadowing is consistent with the poleward increase in epithermal contrast illustrated in Fig. 8 (Carruba and Coradini, 1999).

The production of hydrogen volatiles may also be enhanced on highly illuminated ridges or EFS due to their relatively higher surface exposures to solar wind protons (Farrell et al., 2010). Volatiles may then be mechanically impelled and buried by micrometeorites (Crider and Vondrak, 2002). Though the residence time on highly exposed ridges is likely low, these ridges are in close proximity to PFS cold traps, both spatially and gravitationally, by their being situated directly up-slope. Here, the transport probability of a molecule reaching a cold trap is enhanced as the number of hops and hop distance required to reach the trap are minimized. The lower latitude extent of 50–60°S of hydrogen contrast identified in this paper precludes the possibility that the PFS in this band are wholly in permanent shadow. Instead, the positive epithermal contrasts in that band suggest that PFS act as “cool-traps” that at least temporarily provide locally stable conditions for hydrogen-bearing molecules near the surface. Increased surface roughness on PFS may also enhance very small scale trapping conditions on PFS towards the mid-latitudes. With increased latitude, the number of cool-trap locations and their relative areas increase, thus providing a conditionally longer average probability of survival in near surface conditions than in local surroundings. Epithermal contrasts described in Fig. 8 are correlated evidence of such a process and are consistent with latitude distributions of (H₂O/OH⁻) derived from recent NIR results (Li and Milliken, 2013).

6. Conclusions

Our primary hypothesis that there is a widespread enhancement in hydrogen concentrations that are biased towards the Moon's southern pole-facing slopes is strongly supported by several independent lines of evidence. Co-registered maps of the LEND Collimated Sensor for Epithermal Neutrons, LOLA topography, a surface illumination model as well as a Diviner temperature map were correlated in several cross-cutting experiments to support the conclusions of the paper.

Insolation grids were used to transform the epithermal, temperature and average illumination map rates as a bulk function of slope geomorphology and insolation. The maps were averaged as a function of their underlying topographic slope and slope azimuth angle such that independent pole-facing and equator-facing rates were determined. The suppression of the epithermal rates with

the corresponding illumination and temperature rates on pole-facing slopes is the primary evidence of pole-facing slope hydration in polar latitudes.

Near the poles the suppression of epithermal neutron count rates found on pole-facing slopes was determined to be dependent on the spatial scale of pole-facing slopes and not dependent on the scale of equator-facing slopes. That disparity indicates that the epithermal neutron rates from pole-facing slopes are suppressed and are contrasted with respect to their local surroundings and that the epithermal neutron rates from equator-facing slopes are not. The result strongly indicates that a widespread hydration of pole-facing slopes is occurring in a continuum of spatial scales. Polar equator-facing slopes are non-contrasting and appear to be hydrated to levels that are in equilibrium with their surrounding regions.

Polar regolith temperature contrasts do not explain the suppression of epithermal neutron flux on pole-facing slopes. It is also possible that other geophysical or geochemical alterations to the polar regolith could explain the relative suppression of epithermals on PFS, but these effects must also be maximized at the poles and disappear by the mid-latitudes. Alternative explanations may be more likely in the mid-latitudes where some contrast in the equator-facing slope profiles was observed. In those latitudes temperature, space weathering or mass wasting causes cannot be ruled out as an explanation of the epithermal contrasts between equator-facing and pole-facing slopes.

The evidence is also consistent with several existing lines of research.

- (a) Near the poles, epithermal neutron rates from highly-sloped, pole-facing profiles indicated a baseline ~1% suppression relative to an equivalent equator-facing profile at the south pole indicative of a ~23 ppmw hydrogen PFS enhancement. The result is consistent with the finding of hydration in low illumination conditions on mid-latitude crater slopes found by Pieters et al. (2009).
- (b) The determination of a nearly-symmetric latitude dependent contrast in epithermal neutron count rates on equator and pole-facing slopes suggests that pole-facing slope hydration is occurring over most of the Moon's upper latitudes and provides partial support for upper-latitude hydration findings described by Sunshine et al. (2009), McCord et al. (2011) and Li and Milliken (2013).
- (c) Although these analyses were limited to the south and only considered latitudes 45–90°S, the results showed that the highest contrast (EFS-PFS) in hydrogen concentrations was near the poles, similar to NIR, UV and neutron results (Feldman et al., 1998; Mitrofanov et al., 2012; McCord et al., 2011; Gladstone et al., 2012). Though not evaluated here, the polar results may, at least partly, be driven by the slopes of polar PSR's. However, the existence of epithermal contrast towards lower latitudes 50°S must be primarily derived from pole-facing slopes that are not in PSR.

Future research will consider an identical analysis of the northern hemisphere where low-latitude CSETN coverage is more limited and during the 2-yr of observations, the altitudes are higher, >50-km as compared to the south. The scale of the northern topography relative to the CSETN field-of-view is also smaller, all of which may degrade the epithermal neutron signal-to-noise from hydrated spots (Mazarico et al., 2011). Additionally, CSETN has now accumulated adequate coverage such that it can be split into independent maps, where temporal e.g. diurnal and other surface hydration studies may provide clues to hydrogen production, maintenance and transport processes. A study of the nearly constant illumination and temperature conditions in permanently shadowed regions may provide important clues to hydrogen

volatile production and transport. The methods described in this paper may also be applicable to the correlation of Mercury's neutrons with its topography and its on-going volatile studies, as well as low data-rate volatile mapping studies such as the Lyman Alpha Mapping Project (LAMP) and other small bodies analysis (Lawrence et al., 2012; Gladstone et al., 2012).

Acknowledgments

We lastly thank the Lunar Reconnaissance Orbiter (LRO) project 879 for their ongoing contributions to Lunar science and the NASA 880 Planetary Data System (PDS) for their continued maintenance of 881 these critically essential archives. We also acknowledge Jay Freidlander at the Goddard Space Flight Center for his work on this 882 paper's figures and graphics. Contributions from the Russian co-authors of his paper were supported by grant No. 14-22-00249 of the Russian Scientific Foundation.

Appendix A. Supplementary material

Supplementary data associated with this article can be found, in the online version, at <http://dx.doi.org/10.1016/j.icarus.2014.10.001>.

References

- Arnold, J.R., 1979. Ice in the lunar polar regions. *J. Geophys. Res. – Solid Earth* 84 (B10), 5659–5667.
- Boynton, W.V. et al., 2004. The Mars Odyssey gamma-ray spectrometer instrument suite. *Space Sci. Rev.* 110 (1), 38–83. http://dx.doi.org/10.1007/978-0-306-48600-5_2.
- Boynton, W.V. et al., 2012. High spatial resolution studies of epithermal neutron emission from the lunar poles: Constraints on hydrogen mobility. *J. Geophys. Res. – Planets* 117, E00H33. <http://dx.doi.org/10.1029/2011JE003979> (1–19).
- Carruba, V., Coradini, A., 1999. Lunar cold traps: Effects of double shielding. *Icarus* 142 (2), 402–413.
- Cheek, L.C. et al., 2011. Goldschmidt crater and the Moon's north polar region: Results from the Moon Mineralogy Mapper (M-3). *J. Geophys. Res. – Planets* 116, 1805–1820. <http://dx.doi.org/10.1029/2010JE003702>.
- Chin, G. et al., 2007. Lunar Reconnaissance Orbiter overview: The instrument suite and mission. *Space Sci. Rev.* 129 (4), 391–419. <http://dx.doi.org/10.1007/s11214-007-9153-7>.
- Clark, R.N., 2009. Detection of adsorbed water and hydroxyl on the Moon. *Science* 326 (5952), 562–564. <http://dx.doi.org/10.1126/science.1178105>.
- Clark, R.N., Pieters, C.M., Green, R.O., Boardman, J.W., Petro, N.E., 2011. Thermal removal from near-infrared imaging spectroscopy data of the Moon. *J. Geophys. Res. – Planets* 116, E00G161. <http://dx.doi.org/10.1029/2010JE003751> (1–9).
- Colaprete, A. et al., 2010. Detection of water in the LCROSS ejecta plume. *Science* 330 (6003), 463–468.
- Crider, D.H., Vondrak, R.R., 2000. The solar wind as a possible source for lunar hydrogen. *J. Geophys. Res. – Planets* 105 (E11), 26773–26782. <http://dx.doi.org/10.1029/2000je001277>.
- Crider, D.H., Vondrak, R.R., 2002. Hydrogen migration to the lunar poles by solar wind bombardment of the Moon. *Lunar Explor.* 2000 30 (8), 1869–1874.
- Elphic, R.C., Eke, V.R., Teodoro, L.F.A., Lawrence, D.J., Bussey, D.B.J., 2007. Models of the distribution and abundance of hydrogen at the lunar south pole. *Geophys. Res. Lett.* 34 (13), L12304. <http://dx.doi.org/10.1029/2007GL0200729954> (1–5).
- Fa, W., Weiczorek, M.A., Heggy, E., 2011. Modeling polarimetric radar scattering from the lunar surface: Study on the effect of physical properties of the regolith layer. *J. Geophys. Res. – Planets* 116 (E03005), 1–33. <http://dx.doi.org/10.1029/2010JE003649>.
- Farrell, W.M. et al., 2010. Anticipated electrical environment within permanently shadowed lunar craters. *J. Geophys. Res. – Planets* 115 (E03004), 1–14. <http://dx.doi.org/10.1029/2009JE003464>.
- Feldman, W.C., Boynton, W.V., Drake, D.M., 1993. Planetary neutron spectroscopy from orbit. In: *Remote Geochemical Analysis: Elemental and Mineralogical Composition*. Cambridge University Press, Cambridge, pp. 213–234.
- Feldman, W.C., Maurice, S., Binder, A.B., Barraclough, B.L., Elphic, R.C., Lawrence, D.J., 1998. Fluxes of fast and epithermal neutrons from Lunar Prospector: Evidence for water ice at the lunar poles. *Science* 281 (5382), 1496–1500. <http://dx.doi.org/10.1126/science.281.5382.1496>.
- Feldman, W.C. et al., 2001. Evidence for water ice near the lunar poles. *J. Geophys. Res. – Planets* 106 (E10), 23231–23251. <http://dx.doi.org/10.1029/2000JE001444>.
- Geiger, R., Aron, R.H., Todhunter, P., 1965. The Climate near the Ground. Harvard Univ. Press, Cambridge, MA. <http://dx.doi.org/10.1002/qj.49709339529>.

- Gladstone, G.R. et al., 2012. Far-ultraviolet reflectance properties of the Moon's permanently shadowed regions. *J. Geophys. Res. – Planets* 117 (E12), 1–13. <http://dx.doi.org/10.1029/2011je003913>.
- Goswami, J.N., Annadurai, M., 2008. Chandrayaan-1 mission to the Moon. *Acta Astron.* 63, 1215–1220. <http://dx.doi.org/10.1016/j.actaastro.2008.05.013>.
- Hendrix, A.R. et al., 2012. The lunar far-UV albedo: Indications of hydration and weathering. *J. Geophys. Res. – Planets* 117, E12001. <http://dx.doi.org/10.1029/2012JE004252> (1–8).
- Hibbitts, C.A., Grieves, G.A., Poston, M.J., Dyar, M.D., Alexandrov, A.B., Johnson, M.A., Orlando, T.M., 2011. Thermal stability of water and hydroxyl on the surface of the Moon from temperature programmed desorption measurements of lunar analog materials. *Icarus* 213, 64–72. <http://dx.doi.org/10.1016/j.icarus.2011.02.015>.
- Hurley, D.M. et al., 2012. Modeling of the vapor release from the LCROSS impact: 2. Observations from LAMP. *J. Geophys. Res. – Planets* 117, E00H07. <http://dx.doi.org/10.1029/2011JE003841> (1–15).
- Keihm, S.J., Pieters, K., Langseth, M.G., Chute, J.L., 1973. Apollo-15 measurement of lunar-surface brightness temperatures – Thermal conductivity of the upper 1/2 meters of regolith. *Earth Planet. Sci. Lett.* 19 (3), 337–351.
- Lawrence, D.J. et al., 2011. Sensitivity of orbital neutron measurements to the thickness and abundance of surficial lunar water. *J. Geophys. Res. – Planets* 116, E01002. <http://dx.doi.org/10.1029/2010JE003678> (1–13).
- Lawrence, D.J. et al., 2012. Evidence for water ice near Mercury's north pole from MESSENGER neutron measurements. *Science* 339 (6117), 292–296. <http://dx.doi.org/10.1126/science.1229953>.
- Lawrence, D.J., Peplowski, P.N., Plescia, J.B., Greenhagen, B.T., Maurice, S., Prettyman, T.H., 2014. Lunar highlands bulk hydrogen concentrations. In: *Proceedings of the Lun. Exp. Anal. Group Meeting*. LPI, #3038, Laurel, MD, USA.
- Li, S., Milliken, R.E., 2013. Quantitative mapping of lunar surface hydration with Moon Mineralogy Mapper M3 data. *Lunar Planet. Sci.* #1337, Houston TX, LPI.
- Little, R.C. et al., 2003. Latitude variation of the subsurface lunar temperature: Lunar Prospector thermal neutrons. *J. Geophys. Res. – Planets* 108 (E5), 1–9. <http://dx.doi.org/10.1029/2001JE001497>.
- Litvak, M.L. et al., 2008. The dynamic albedo of neutrons (DAN) experiment for NASA's 2009 Mars Science Laboratory. *Astrobiology* 8 (3), 605–612. <http://dx.doi.org/10.1089/ast.2007.0157>.
- Litvak, M.L. et al., 2012a. Global maps of lunar neutron fluxes from the LEND instrument. *J. Geophys. Res. – Planets* 117, E00H22. <http://dx.doi.org/10.1029/2011JE003949> (1–18).
- Litvak, M.L. et al., 2012b. LEND neutron data processing for the mapping of the Moon. *J. Geophys. Res. – Planets* 117, E00H32. <http://dx.doi.org/10.1029/2011JE004035> (1–21).
- Lofgren, T.L., 1993. The first lunar outpost: The design reference mission and a new era in lunar science. NASA Technical Report. NASA/JSC.
- Lucey, P.G., Neumann, G.A., Riner, M.A., Mazarico, E., Smith, D.E., Zuber, M.T., Paige, D.A., Bussey, D.B., Cahill, J.T., McGovern, A., Isaacson, P., Corley, L.M., Torrence, M.H., Melosh, H.J., Head, J.W., Song, E., 2014. The global albedo of the Moon at 1064 nm. *J. Geophys. Res. – Planets* 119, 1665–1679. <http://dx.doi.org/10.1002/2013JE004592>.
- Maurice, S., Lawrence, D.J., Feldman, W.C., Elphic, R.C., Gasnault, O., 2004. Reduction of neutron data from Lunar Prospector. *J. Geophys. Res. – Planets* 109, E07S04. <http://dx.doi.org/10.1029/2003JE002208> (1–40).
- Mazarico, E., Neumann, G.A., Smith, D.E., Zuber, M.T., Torrence, M.H., 2011. Illumination conditions of the lunar polar regions using LOLA topography. *Icarus* 211, 1066–1081. <http://dx.doi.org/10.1016/j.icarus.2010.10.030>.
- McClanahan, T. et al., 2012. Correlated observations of epithermal neutrons and polar illumination models from orbital neutron detectors. *Lunar Planet. Sci.* 43, #2341.
- McClanahan, T. et al., 2013. Bulk insolation models as predictors for locations of high lunar hydrogen concentration. *Lunar Planet. Sci.* #2374.
- McCord, T.B. et al., 2011. Sources and physical processes responsible for OH/H₂O in the lunar soil as revealed by the Moon Mineralogy Mapper (M-3). *J. Geophys. Res. – Planets* 116, E00G05. <http://dx.doi.org/10.1029/2010JE003711> (1–22).
- Mitrofanov, I. et al., 2008. Experiment LEND of the NASA Lunar Reconnaissance Orbiter for high-resolution mapping of neutron emission of the Moon. *Astrobiology* 8 (4), 793–804. <http://dx.doi.org/10.1089/ast.2007.0158>.
- Mitrofanov, I.G. et al., 2010a. Lunar Exploration Neutron Detector for the NASA Lunar Reconnaissance Orbiter. *Space Sci. Rev.* 150 (1–4), 183–207. <http://dx.doi.org/10.1007/s11214-009-9608-4>.
- Mitrofanov, I.G. et al., 2010b. Hydrogen mapping of the lunar south pole using the LRO neutron detector experiment LEND. *Science* 330 (6003), 483–486. <http://dx.doi.org/10.1126/science.1185696>.
- Mitrofanov, I. et al., 2012. Testing polar spots of water-rich permafrost on the Moon: LEND observations onboard LRO. *J. Geophys. Res. – Planets* 117, E00H27. <http://dx.doi.org/10.1029/2011JE003956> (1–14).
- Nozette, S. et al., 1996. The Clementine bistatic radar experiment. *Science* 274 (5292), 1495–1498. <http://dx.doi.org/10.1126/science.274.5292.1495>.
- Paige, D.A. et al., 2010a. The Lunar Reconnaissance Orbiter Diviner Lunar Radiometer Experiment. *Space Sci. Rev.* 150 (1–4), 125–160. <http://dx.doi.org/10.1007/s11214-009-9259-2>.
- Paige, D.A. et al., 2010b. Diviner Lunar Radiometer Experiment observations of cold traps in the Moon's south polar region. *Science* 330 (6003), 479–482. <http://dx.doi.org/10.1126/science.1187726>.
- Pieters, C.M. et al., 2009. Character and spatial distribution of OH/H₂O on the surface of the Moon seen by M3 on Chandrayaan-1. *Science* 326 (5952), 568–572. <http://dx.doi.org/10.1126/science.1178658>.
- Prettyman, T.H. et al., 2011. Dawns gamma-ray and neutron detector. *Space Sci. Rev.* 183 (1–4), 351–459. <http://dx.doi.org/10.1007/s11214-011-9682-0>.
- Ritter, D.F., Kochel, R.C., 2002. *Process Geomorphology*, fourth ed. Waveland Press Inc.
- Rosenburg, M. et al., 2011. Global surface slopes and roughness of the Moon from the Lunar Orbiter Laser Altimeter. *J. Geophys. Res. – Planets* (1991–2012) 116 (E2), E02001. <http://dx.doi.org/10.1029/2010JE003716> (1–11).
- Sanders, G.B., Larson, W.E., 2010. Integration of in-situ resource utilization into lunar/Mars exploration. *Adv. Space. Res.* 47 (1), 20–29. <http://dx.doi.org/10.1016/j.asr.2010.08.020>.
- Sanin, A.B. et al., 2012. Testing lunar permanently shadowed regions for water ice: LEND results from LRO. *J. Geophys. Res. – Planets* 117, E00H26. <http://dx.doi.org/10.1029/2011JE003971> (1–13).
- Schorghofer, N., Taylor, G.J., 2007. Subsurface migration of H₂O at lunar cold traps. *J. Geophys. Res. – Planets* 112 (E2), E02010. <http://dx.doi.org/10.1029/2006JE002779> (23231–23251).
- Siegler, M.A., Bills, B.G., Paige, D.A., 2011. Effects of orbital evolution on lunar ice stability. *J. Geophys. Res. – Planets* (1991–2012) 116 (E3), E03010. <http://dx.doi.org/10.1029/2010JE003652> (1–18).
- Simpson, R.A., Tyler, G.L., 1999. Reanalysis of Clementine bistatic radar data from the lunar south pole. *J. Geophys. Res. – Planets* (1991–2012) 104 (E2), 3845–3862. <http://dx.doi.org/10.1029/1998JE000038>.
- Smith, D.E. et al., 2010. The Lunar Orbiter Laser Altimeter investigation on the Lunar Reconnaissance Orbiter mission. *Space Sci. Rev.* 150 (1–4), 209–241. <http://dx.doi.org/10.1007/s11214-009-9512-y>.
- Starukhina, L.V., 2000. On the origin of excess hydrogen at the lunar poles. *Solar Syst. Res.* 34 (3), 215–219.
- Sunshine, J.M. et al., 2009. Temporal and spatial variability of lunar hydration as observed by the Deep Impact spacecraft. *Science* 326 (5952), 565–568. <http://dx.doi.org/10.1126/science.1179788>.
- Urey, H.C., 1952. *The Planets: Their Origin and Development*. Yale Univ. Press, New Haven, CT.
- Vasavada, A.R., Paige, D.A., Wood, S.E., 1999. Near-surface temperatures of Mercury and the Moon and the stability of polar ice deposits. *Icarus* 141 (2), 179–193.
- Vincendon, M., Forget, F., Mustard, J., 2010. Water ice at low to midlatitudes on Mars. *J. Geophys. Res. – Planets* 115, E10001. <http://dx.doi.org/10.1029/2010JE003584> (1–13).
- Vondrak, R.R., Keller, J.W., Russell, C.T., 2010. Lunar Reconnaissance Orbiter mission – Preface. *Space Sci. Rev.* 150 (1–4), 1–2. <http://dx.doi.org/10.1007/s11214-010-9631-5>.
- Watson, K., Brown, H., Murray, B., 1961. Behavior of volatiles on lunar surface. *J. Geophys. Res.* 66 (9), 3033–3035. <http://dx.doi.org/10.1029/JZ066i009p03033> (1–13).
- Zellar, E.J., Ronca, L.B., Levy, P.W., 1966. Proton-induced hydroxyl formation on the lunar surface. *J. Geophys. Res.* 71, 4855–4860.
- Zuber, M.T. et al., 2012. Constraints on the volatile distribution within Shackleton crater at the lunar south pole. *Nature* 486, 378–381. <http://dx.doi.org/10.1038/nature11216>.